Journal of Power Sources 248 (2014) 265–272

Contents lists available at ScienceDirect

Journal of Power Sources

journal homepage: www.elsevier.com/locate/jpowsour

Mesoporous $Li_4Ti_5O_{12}$ nanoclusters as high performance negative electrodes for lithium ion batteries

Li Sun, Jiaping Wang*, Kaili Jiang, Shoushan Fan

Department of Physics and Tsinghua-Foxconn Nanotechnology Research Center, Tsinghua University, Beijing, PR China

HIGHLIGHTS

- Synthesis of mesoporous $Li_4Ti_5O_{12}$ nanoclusters by a solution-based method.
- Simple synthetic route and low-temperature heat treatment.
- The $Li_4Ti_5O_{12}$ electrode delivers excellent cycling and rate performance.

GRAPHICAL ABSTRACT

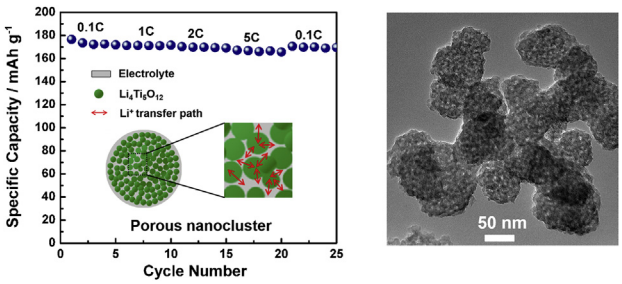

ARTICLE INFO

Article history:
Received 11 July 2013
Received in revised form
3 September 2013
Accepted 9 September 2013
Available online 23 September 2013

Keywords:
Lithium titanate
Nanocluster
Mesoporosity
Lithium ion battery

ABSTRACT

Porous $Li_4Ti_5O_{12}$ nanoclusters with high surface area are synthesized by a facile solution-based method followed by low-temperature calcination. The $Li_4Ti_5O_{12}$ nanoclusters present the key characteristics needed to serve as high-performance negative electrodes for lithium ion batteries, including nano-sized dimension of the $Li_4Ti_5O_{12}$ clusters (50–100 nm) for short ion and electron transfer path, and high surface area (142 $m^2\ g^{-1}$) with mesoporosity (pore diameter 2–6 nm) for easy access to the electrolyte and efficient ion transport. Based on these characteristics, the $Li_4Ti_5O_{12}$ electrode delivers an initial capacity of 173 mAh g^{-1} at the rate of 0.5 C, comparable to its theoretical capacity. Excellent cycling stability at high rates is achieved in the $Li_4Ti_5O_{12}$ electrode, offering potential to serve as a negative electrode material for high rate lithium ion battery applications.

1. Introduction

As the environmental problems and energy crisis become more and more serious, there has been a growing appreciation to develop clean and renewable energy sources to substitute the traditional fossil fuels. Lithium ion batteries (LIBs) are among one of the widely utilized energy storage sources, which provide environmental compatibility and high energy density for the next generation electronic devices. For years, efforts have been made to improve the power density, cycling stability, and operating safety of the LIBs in order to meet the requirement of hybrid electric vehicles (HEVs). There are several issues associated with the graphite negative electrodes for commercial LIBs. First, the potential plateau of graphite negative electrodes is very close to that of lithium. The formation of dendritic lithium is still unavoidable, which can cause safety problems [1,2]. Secondly, a lithium conducting solid–electrolyte interface (SEI) layer is usually formed on the surface of graphite below 1.0 V versus Li/Li^+ during cycling, which results in irreversible capacity loss [3]. Thirdly, the volume change during the lithium insertion and extraction is relatively large in graphite (9%) [3]. For comparison, lithium titanate ($Li_4Ti_5O_{12}$) with a spinel structure turns out to be a promising candidate for the negative

* Corresponding author. Tel.: +86 10 62796007; fax: +86 10 62792457.
E-mail address: jpwang@tsinghua.edu.cn (J. Wang).

0378-7753/$ – see front matter © 2013 Elsevier B.V. All rights reserved.
http://dx.doi.org/10.1016/j.jpowsour.2013.09.041

electrode materials in LIBs [4–7]. The spinel $Li_4Ti_5O_{12}$ is a stable phase of the Li_2O–TiO_2 system, which allows the insertion of three Li atoms per formula unit at a potential of 1.5 V [8,9] on the basis of a reversible phase transition between spinel structure and NaCl structure [10,11]. This mechanism leads to the reduction of three Ti (IV) atoms out of five, corresponding to a theoretical capacity of 175 mAh g^{-1} [12]. The working voltage window of $Li_4Ti_5O_{12}$ is in the range of 1.0–2.5 V. Such higher working potentials than graphite fulfill the urgent requirement to avoid the safety problems caused by the formation of dendritic lithium. Moreover, the volumetric variation of $Li_4Ti_5O_{12}$ during the charge/discharge processes is almost negligible [7]. The zero-strain feature of $Li_4Ti_5O_{12}$ allows excellent structural stability and cycling reversibility during the charge/discharge processes [5–7]. All these characteristics, including the improved safety and structure stability during the charge/discharge process, contribute to the excellent cycling performance and great promise for high rate LIB applications.

Though possessing all these advantages, $Li_4Ti_5O_{12}$ also suffers from the problem of poor capacity at high rates due to its low electronic conductivity. The electronic transportation and rate performance in $Li_4Ti_5O_{12}$ electrodes can be improved by coating the $Li_4Ti_5O_{12}$ phase with a conductive shell such as Ag or carbon [13–16]. While at the same time, the synthesis of such composites usually needs delicate controls of reaction conditions such as atmosphere, temperature, pH, *etc*., and complex procedures are needed to form a conformal conductive shell. Besides, the content of the active material in the electrode is decreased to a certain extent due to the electrochemically inactive conducting coating, resulting in a relatively low specific capacity. Microstructural modification by controlling the grain size and morphology of the $Li_4Ti_5O_{12}$ particles has also been shown effective in improving the capacity at high rates. The reduction in the grain size can lead to a shorter lithium ion diffusion path, a higher electrode/electrolyte contact surface area, and thus better rate performance [17–19]. Porous electrode materials have also attracted much attention due to their large contact area with the electrolyte and the possibility to form a three-dimensional conductive network filled within the porous active material [3]. Particularly, mesoporous materials are preferred in LIB electrodes. Compared to microporous and macroporous materials, mesoporous material possesses a balanced pore size (2–50 nm) and offers large surface area and short transfer paths for both electrons and ions to migrate rapidly, thus benefiting both the ionic and electronic transportation and leading to a superior rate performance [3,20,21].

Our work focuses on the control of the microstructure of $Li_4Ti_5O_{12}$ particles and the improvement of their performance as a negative electrode material. A facile method to prepare well-crystallized $Li_4Ti_5O_{12}$ nanoclusters with mesoporosity is introduced. The synthesized $Li_4Ti_5O_{12}$ powder combines the advantages of mesoporosity and nano-dimension and presents excellent cycling stability and rate performance.

2. Experiment

2.1. Synthesis of the mesoporous $Li_4Ti_5O_{12}$ nanoclusters

$Li_4Ti_5O_{12}$ nanoclusters were synthesized by a facile solution-based direct-synthesis-from-solution (DSS) method [22] followed by low-temperature calcination with lithium hydroxide monohydrate ($LiOH{\cdot}H_2O$, Alfa Aesar, ACS, 98% purity) and tetrabutyl titanate $C_{16}H_{36}O_4Ti$, Alfa Aesar, ACS, 98% purity) as the starting materials. The schematic of the formation process is shown in Fig. 1(a). In a typical process, 0.04 mol lithium hydroxide monohydrate was dissolved into 20 mL deionized water to form the base solution. 0.055 mol tetrabutyl titanate was dissolved in 30 mL ethanol to form a clear solution. When the base solution was heated to 80 °C, the $C_{16}H_{36}O_4Ti$ solution was added into the base solution under normal pressure and then stirred quickly. An instantaneous formation of white precipitation was observed when adding $C_{16}H_{36}O_4Ti$ solution into a $LiOH{\cdot}H_2O$ base solution at 80 °C, accompanied by the change of the pH value from nearly 14 caused by the strongly alkaline feature of $LiOH{\cdot}H_2O$ solution to around 7 after the two reactants are mixed together. After the reaction was completed, the precipitation was collected and dried at 60 °C for 24 h to obtain the precursor powders. Then the precursor powders were calcined at the temperatures of 400 °C, 600 °C, and 800 °C to allow further crystallization of $Li_4Ti_5O_{12}$. It should be mentioned that a heat treatment of the precursor powder at a lower

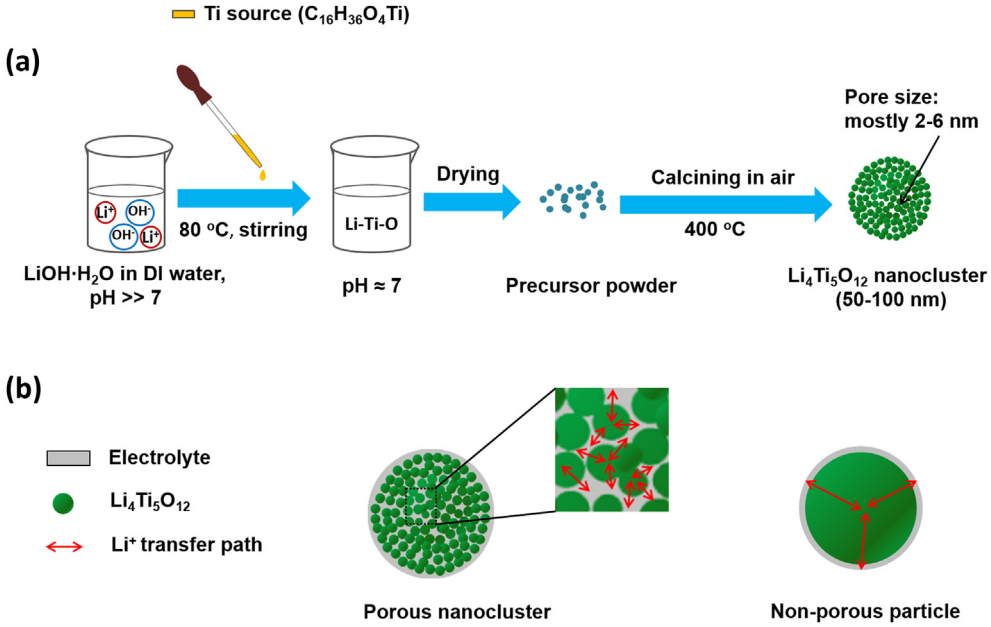

Fig. 1. Schematic illustration of (a) the formation process of mesoporous $Li_4Ti_5O_{12}$ nanoclusters via a solution-based method followed by a low-temperature calcination in air; (b) the shortened lithium ion transfer path in the porous nanoclusters.

temperature, i.e., 350 °C, was also conducted, while no spinel $Li_4Ti_5O_{12}$ phase was obtained.

2.2. Structure, morphology, and porosity characterization

The crystalline structures of the powders obtained at different calcination temperatures were characterized by X-ray diffraction (XRD) using a diffractometer (Rigaku, Cu Kα radiation). The diffraction patterns were recorded at room temperature in the 2θ range from 10° to 90°.

The morphology and particle size were characterized by transmission electron microscopy (TEM, FEI Tecnai F20). The Brunauer–Emmett–Teller (BET) measurements were performed on a surface area and porosity analyzer (ASAP 2020) to examine the N_2 adsorption/desorption behavior and specific surface area of the sample.

2.3. Electrochemical analysis

The electrochemical performance of the prepared $Li_4Ti_5O_{12}$ particles with different calcination temperatures, as well as the commercial $Li_4Ti_5O_{12}$ powder (Shenzhen Tianjiao Technology Co. Ltd, China) were examined under the same condition. Electrochemical performance measurements were performed using 2016 coin-type half-cells that were assembled in a glove box filled with protective argon gas (M. Braun inert gas systems Co. Ltd., Germany) with $Li_4Ti_5O_{12}$ as the working electrode and pure lithium foil as the reference electrode. The $Li_4Ti_5O_{12}$ slurry was prepared by thoroughly mixing a *N*-methyl-2-pyrrolidine solution with the active material, conductive Super P, and a poly(vinyl difluoride) binder in a weight ratio of 80:10:10. Afterward, the slurry was deposited on a copper foil (10 μm thick) followed by drying in a vacuum oven at 120 °C overnight. A polypropylene film (Celgard 2400) was used to separate the positive and the negative electrodes. A 1 M $LiPF_6$ solution in ethylene carbonate (EC) and diethyl carbonate (DEC) mixed at a weight ratio of 1:1 was adopted as electrolyte in the test cells. The cyclic voltammetry scans and electrochemical impedance spectroscopy (EIS) analysis were performed with a 2-electrode system using a Potentiostat/Galvanostat (EG&G Princeton Applied Research 273A). The discharge and charge measurements were made on a Land battery test system (Wuhan Land Electronic Co., China) in a voltage window of 1.0–2.5 V at different rates at room temperature.

3. Results and discussion

3.1. X-ray diffraction studies

The structures of the precursor powder and the $Li_4Ti_5O_{12}$ particles obtained under different heat treatments between 400 °C and 800 °C were examined by X-ray diffraction (XRD). Fig. 2(a) shows the XRD pattern of the as-prepared precursor powder, which can be indexed as a combination of rock-salt type $LiTiO_2$ and Li_2CO_3. The formation of the $LiTiO_2$ phase indicates that the raw materials, $LiOH{\cdot}H_2O$ and $C_{16}H_{36}O_4Ti$, reacted when mixed at the temperature of 80 °C. The presence of Li_2CO_3 mainly results from the reaction between the reactant $LiOH{\cdot}H_2O$ and CO_2 in air. The relatively high background of the curve indicates the presence of amorphous phase which might result from the retention of the hydrolysis product of $C_{16}H_{36}O_4Ti$. The XRD pattern of the precursor powder calcined at 400 °C shown in Fig. 2(b) gives good agreement with the standard spinel $Li_4Ti_5O_{12}$ phase with its peak positions and relative intensities marked by the column lines (JCPDS card PDF#72-0426), suggesting the formation of the well crystallized $Li_4Ti_5O_{12}$ phase. The wide peaks of the synthesized $Li_4Ti_5O_{12}$ indicate the small grain

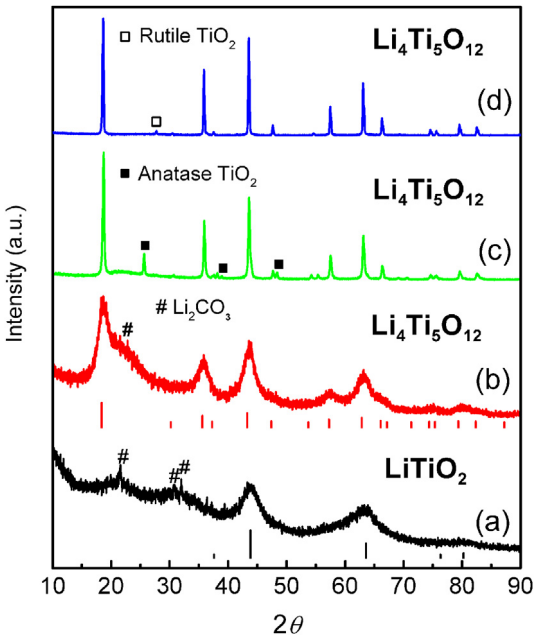

Fig. 2. The XRD patterns of (a) the as-prepared precursor powder as a combination of $LiTiO_2$ and Li_2CO_3, and (b)–(d) the $Li_4Ti_5O_{12}$ particles after heat treatments at 400 °C, 600 °C, and 800 °C. The column lines in figures (a) and (b) present the standard peak positions and intensities of $LiTiO_2$ and $Li_4Ti_5O_{12}$, respectively.

size of the particles, and the second phase in the sample can be indexed as Li_2CO_3 with its characteristic peak at 21.3°, corresponding to the lattice plane of (110) (JCPDS card, PDF#72-1216). Similar to the precursor powder shown in Fig. 2(a), the 400 °C treated powder also shows a background in the XRD pattern, which results from the amorphous hydrolysis product of $C_{16}H_{36}O_4Ti$. As the calcination temperature is increased further to 600 °C, the peaks of $Li_4Ti_5O_{12}$ become sharper as shown in Fig. 2(c), demonstrating further crystallization and grain growth at elevated temperature. The impurity of Li_2CO_3 becomes less obvious and the anatase TiO_2 begins to form in the sample due to the pyrolysis of the hydrolysis product of $C_{16}H_{36}O_4Ti$ at elevated temperatures. When the heat-treatment temperature is increased to 800 °C, the main phase is still $Li_4Ti_5O_{12}$. The anatase TiO_2 reacts with Li_2CO_3 to form $Li_4Ti_5O_{12}$, while the excess anatase TiO_2 phase transfers into rutile phase as shown in Fig. 2(d).

The crystallite sizes of the LTO samples calcined at different temperatures were calculated via the Scherrer's equation based on the line broadening effect, i.e.:

$$d_x = \frac{K\lambda}{\beta\cos\theta} \quad (1)$$

where d_x is the crystallite size, K is 0.89 as the shape factor, λ is the wavelength of X-ray, β is the true half-peak width and θ is the diffraction angle of the peak (in degrees). Through the XRD profiles of the (400) plane of the samples calcined at different temperatures, the crystallite size and lattice parameters were calculated. The results show that the LTO samples calcined at 400, 600 and 800° possess the crystalline sizes of 13.7, 112.9, and 147.2 nm, respectively.

3.2. Morphology of the $Li_4Ti_5O_{12}$ particles

The morphology change of the $Li_4Ti_5O_{12}$ particles at various calcination temperatures were further examined by TEM. Fig. 3(a) and (b) shows the TEM and HRTEM images of the particles calcined

at 400 °C. Nanoclusters with a uniform diameter of 50–100 nm are observed in the sample (Fig. 3(a)). These nanoclusters are consisted of densely packed and interconnected grains. Clear grain lattice can be found in the HRTEM image shown in Fig. 3(b), indicating that these $Li_4Ti_5O_{12}$ nanoclusters are well crystallized. Two typical lattice distances of 0.48 nm and 0.21 nm are marked in the image, corresponding to the (111) and (400) planes of the spinel $Li_4Ti_5O_{12}$. Nano-sized pores are observed within the $Li_4Ti_5O_{12}$ nanoclusters, as indicated by the red dotted circles in Fig. 3(b). These nanoclusters are expected to allow more efficient electrolyte infiltration, provide shortened lithium ion transfer pathways and facilitate faster ionic transportation during the lithiation and delithiation processes as illustrated in Fig. 1(b). When the sample undergoes a higher-temperature calcination at 600 °C, the porous structure is eliminated and these nanospheres merge into larger nanoparticles with 50–100 nm in dimension (Fig. 3(c)). Heat treatment at 800 °C causes further grain growth with particle size increased to around 200 nm (Fig. 3(d)). According to the inset of Fig. 3(c) and (d), both kinds of samples calcined at 600 °C and 800 °C are identified as well-crystallized $Li_4Ti_5O_{12}$ phase with a standard grain lattice distance of 0.48 nm that can be assigned to the (111) plane of the spinel $Li_4Ti_5O_{12}$. The crystalline sizes observed from the TEM images are in accordance with those calculated from the XRD profiles.

3.3. Mesoporous structures of the $Li_4Ti_5O_{12}$ particles

A statistical analysis of the pore size distribution of the 400°C-calcined $Li_4Ti_5O_{12}$ particles based on the TEM images reveals that the pores within the nanoclusters possess a diameter of 2–6 nm, and about half of the pores show a diameter of 3–4 nm (Fig. 4(a)). The average diameter of the pores is 4.1 nm, indicating a typical mesoporous structure in the particles. The nano-sized porous microstructure of the $Li_4Ti_5O_{12}$ samples calcined at 400 °C was further examined by Brunauer–Emmett–Teller (BET) measurements. According to the BET results, the $Li_4Ti_5O_{12}$ sample calcined at 400 °C with porous structure exhibits a large BET surface area of 142 $m^2\ g^{-1}$, which is much higher than those of the samples calcined at 600 °C (18 $m^2\ g^{-1}$) and 800 °C (5.6 $m^2\ g^{-1}$). Moreover, the BET surface area of the $Li_4Ti_5O_{12}$ sample calcined at 400 °C is higher or comparable to other $Li_4Ti_5O_{12}$ porous structures reported in literature [21,23]. The pore size distribution of the sample based on the BET measurement is shown in Fig. 4(b). The inset of Fig. 4(b) gives the nitrogen adsorption–desorption isotherm curve of the sample, which can be sorted into type IV characterized by the hysteresis of the adsorption and desorption curves according to the IUPAC classification. The distinctive hysteresis is found in the relative pressure (P/P_0) range of 0.3–1.0, which can be attributed to the mesopores in the porous stacking of $Li_4Ti_5O_{12}$ particles. At the same time, the sharp increase of the adsorption curve near the relative pressure of 1.0 indicated the existence of macropores in the sample [24]. The corresponding Barrett–Joyner–Halenda (BJH) desorption pore size distribution in Fig. 4(b) shows that the pores at the major peak position with a diameter of 2.0–5.9 nm contribute to 45.5% of the overall pore volume (Table S1), in good agreement with the statistical analysis from the TEM images with half of the pores possessing a diameter of 3–4 nm. The maximum pore

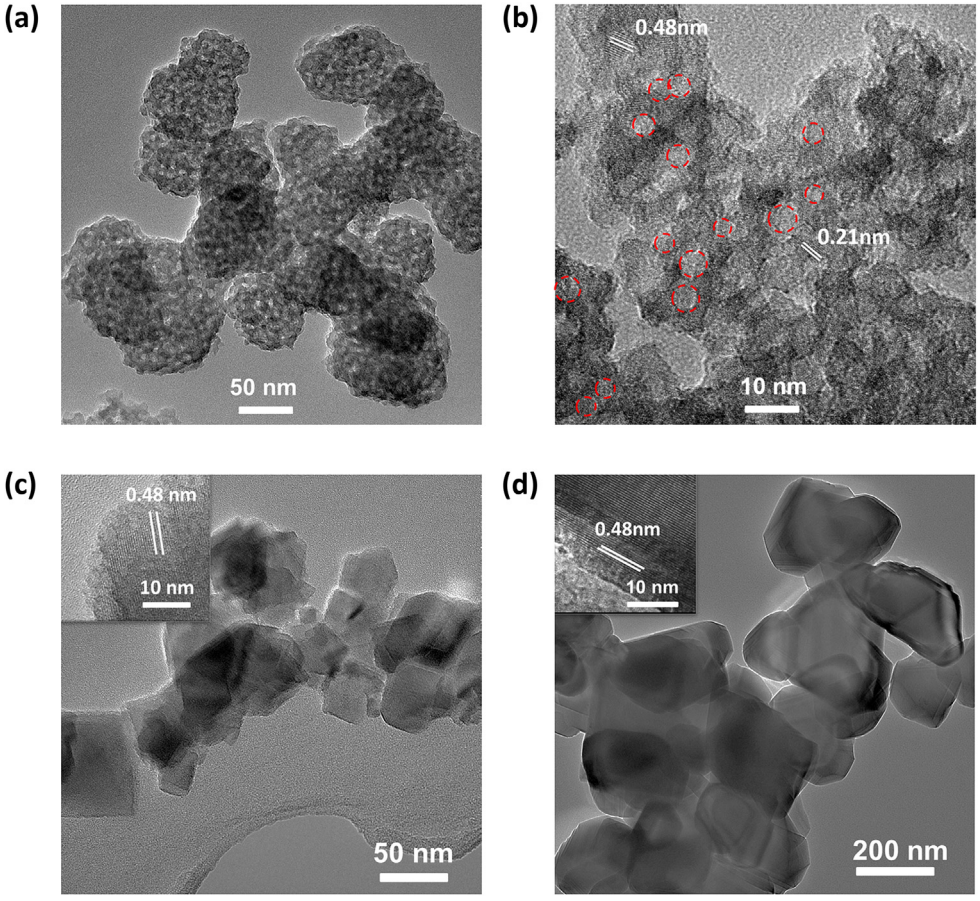

Fig. 3. TEM and HRTEM images of the $Li_4Ti_5O_{12}$ particles after heat treatments at (a) 400 °C at low magnification (b) 400 °C at high magnification, (c) 600 °C, and (d) 800 °C. The red dotted circles in figure (b) mark the pores within the LTO clusters. (For interpretation of the references to colour in this figure legend, the reader is referred to the web version of this article.)

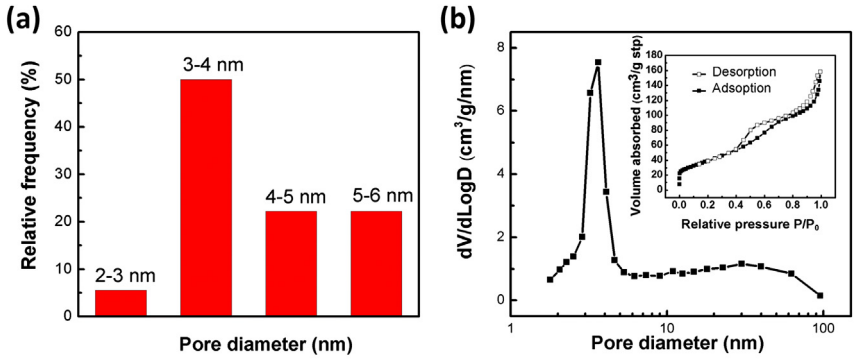

Fig. 4. Pore size distribution in the $Li_4Ti_5O_{12}$ particles after heat treatment at 400 °C based on (a) TEM analysis and (b) BET measurement, with an inset of the N_2 adsorption–desorption isotherm loop.

volume is achieved at the diameter of 3.61 nm. A second mild peak is located at the pore diameter of 29.8 nm, which may be caused by the interspace among the $Li_4Ti_5O_{12}$ nanoclusters. Macropores are also found in the pore diameter of 50–100 nm region, indicating a combined mesoporous and macroporous structure in the sample. Both the TEM image analysis and the BET results suggest the highly porous structure of the $Li_4Ti_5O_{12}$ powders calcined at 400 °C. The mesoporosity within the $Li_4Ti_5O_{12}$ nanoclusters contributes to the large specific surface area of the sample, which provides enhanced lithium ion reaction sites for the electrode material. Besides, the porous microstructure can also provide large electrode–electrolyte interfacial area and efficient ionic transportation, which is of significance to serve as a negative electrode material for the high-rate performance in LIBs.

3.4. Electrochemical properties of the $Li_4Ti_5O_{12}$ particles

The electrochemical properties of the $Li_4Ti_5O_{12}$ sample calcined at 400 °C (labeled as LTO-400) with a highly porous structure were thoroughly studied at room temperature as a negative electrode material in LIBs. When the Li|$Li_4Ti_5O_{12}$ cell was assembled and let stand for 4 h, the first cyclic voltammogram(CV) curves and electrochemical impedance spectroscopy (EIS) curves as "before cycling". Then the cell underwent one discharge/charge cycle at 1 C and the second curves were obtained as "after one cycle". After that, four more discharge/charge cycles at 1 C were conducted to the cell and the third curves were obtained as "after 5 cycles". Fig. 5(a) shows the typical cyclic voltammogram curves of the porous LTO between 1.0 V and 2.5 V with a scanning rate of 0.1 mV s^{-1}. The sample displays only one pair of oxidation/reduction peaks, indicating that single-phase transition occurs over the whole electrochemical process. The downward cathodic and the upward anodic peaks can be attributed to intercalation and deintercalation of Li^+, corresponding to the reduction and oxidation of titanium cation, respectively. The electrochemical processes can be described as:

$$Li_4Ti_5O_{12} + 3Li^+ + 3e^- \leftrightarrow Li_7Ti_5O_{12} \quad (2)$$

The peak currents were achieved at the 1.68 V, 1.67 V, and 1.67 V for the anodic scans, and 1.46 V, 1.47 V, and 1.47 V for the cathodic scans before cycling, after the 1st cycle, and after the 5th cycle, respectively. A shoulder appeared in the cathodic peak. Such split cathodic peaks might be related to the spinel/rock-salt transition products between the $Li_4Ti_5O_{12}$ and $Li_7Ti_5O_{12}$ phases. [25,26] The cyclic voltammograms before and after cycling are almost overlapped, indicating excellent cycle reversibility. The sharp oxidation/reduction peaks also demonstrate that the $Li_4Ti_5O_{12}$ electrode possesses fast kinetics toward Li^+ intercalation and deintercalation, which might benefit the high-rate cycling performance. [27,28] The peak current slightly increased after cycling, which might be associated with the enhanced wetting between the $Li_4Ti_5O_{12}$ electrode and electrolyte and the decrease of charge transfer resistance during cycling. EIS analysis was also performed to understand the cycling mechanism (Fig. 5(b)). The diameter of the depressed semicircle in the high frequency range of the EIS spectra refers to the charge transfer resistance. After cycling, the diameter of the semicircle decreased, indicating a decrease of the charge transfer

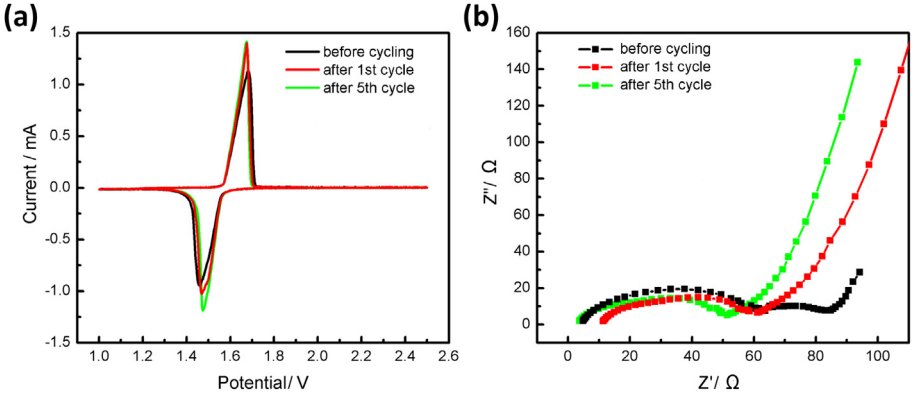

Fig. 5. (a) The cyclic voltammogram curves and (b) the electrochemical impedance spectroscopy data of the LTO-400 sample before cycling, after one cycle, and after five cycles. The scanning rate in the CV curve is set at 0.1 mV s^{-1}.

resistance at the $Li_4Ti_5O_{12}$–electrolyte interface. These results further confirm that the decrease of the charge transfer resistance, which might be related to the enhanced wetting between the $Li_4Ti_5O_{12}$ electrode and electrolyte, is responsible for the increase of the peak current in the CV curves after cycling.

The LTO-400 battery was cycled at various charge/discharge rates to investigate its cycling behavior. Fig. 6(a) shows the charge/discharge curves of the LTO-400 sample between 1.0 V and 2.5 V at the rate of 0.5 C. The curves were recorded in the 1st, 20th, 40th, and 60th charge–discharge cycle. Clear plateaus are found at around 1.58 V and around 1.54 V for the charging and discharging, corresponding to the cathodic and anodic processes, respectively. The difference between the charge and discharge plateau potentials is only 40 mV, indicating the low extent of polarization of the electrode. The reversible discharge capacity of cycle 1, 20, 40, and 60 are 173, 171, 169 and 168 mAh g^{-1} respectively. These capacity values are comparable to the theoretical capacity of spinel $Li_4Ti_5O_{12}$. No obvious capacity fading is observed up to 60 cycles, revealing good cycling stability. The LTO-400 electrode was also cycled at higher charge/discharge rates of 1 C, 2 C, and 5 C. Fig. 6(b) records the charge/discharge curves of the 1st cycles at the rates of 0.5 C, 1 C, 2 C, and 5 C. The charge and discharge rates were kept the same during cycling. At the rates ranging from 0.5 C to 2 C, the discharge plateau potentials are all near 1.50 V. However, when the charge/discharge rate is increased further to 5 C, the discharge plateau potential drops to about 1.33 V, revealing increased polarization of the electrode at higher rates. As the charge–discharge rate increases, the capacity decreases from 173 mAh g^{-1} (0.5 C) to 158 (1 C), 141 (2 C), and 137 (5 C) mAh g^{-1}, respectively. Note that the discharge capacity at 5 C is still about 80% of that obtained at 0.5 C. These data demonstrate a good high-rate performance of the porous LTO-400 sample. Such stable cycling properties of LTO-400 at high charge/discharge rates can be attributed to the mesoporous microstructures in the sample that allow more flexibility and structure stability during the charge/discharge process (Fig. 1(b)). Besides, the small dimension of the nanoclusters also results in shorter distance for electron and lithium ion diffusion in $Li_4Ti_5O_{12}$ cluster, and thus benefits the high rate performance.

The specific capacity as a function of cycling numbers for the LTO-400 sample is given in Fig. 7(a). The cycling was conducted up to 60 cycles in the voltage window between 1.0 and 2.5 V at the charge–discharge rate of 0.5 C. For comparison, the samples calcined at 600 °C and 800 °C (labeled as LTO-600 and LTO-800) and a commercially $Li_4Ti_5O_{12}$ sample (labeled as LTO-commercial) were also tested. As expected, the porous LTO-400 sample presents a superior initial discharge capacity of 173 mAh g^{-1}, which is larger than 166 mAh g^{-1} for LTO-600, 167 mAh g^{-1} for LTO-800, and 152 mAh g^{-1} for LTO-commercial. These results confirm that the high capacity of the LTO-400 sample is attributed to its special structure including both small particle size and mesoporosity. The tap density of the LTO-400 sample was 0.76 g cm^{-3}, comparable to that of LTO nanoparticles reported in literature (around 0.8 g cm^{-3} [29]), resulting in a volumetric capacity of 131 mAh cm^{-3}. Further work will be done to optimize the microstructure of the $Li_4Ti_5O_{12}$ particles to increase the tap density and the volumetric capacity of $Li_4Ti_5O_{12}$. It should be noted that the particle sizes of the LTO-600 sample (50–100 nm) and the LTO-800 sample (200 nm) are smaller than the commercial LTO powder (D_{50} = 730 nm). Therefore, larger capacities are also obtained in the LTO-600 and LTO-800 samples than the commercial LTO powder. Apart from the large initial capacities, these LTO-400, LTO-600, and LTO-800 samples also show good cycling stability and their capacities are 168, 146, and 145 mAh g^{-1} respectively after 60 cycles, with small fading rates of 0.08 (0.048%), 0.33 (0.201%) and 0.37 (0.22%) mAh g^{-1} per cycle, respectively.

The rate performances of the obtained $Li_4Ti_5O_{12}$ particles were also examined. Fig. 7(b) shows the rate capability of the $Li_4Ti_5O_{12}$ negative electrodes upon cycling at a constant discharge rate of 0.1 C, with varied charge rates of 0.1 C, 1 C, 2 C, and 5 C. At each current density, the batteries were tested for 5 cycles to ensure the reliability of their performance. For each of the batteries, the specific capacity is stable at a constant charge/discharge rate, while changes in current density lead to a stepwise dependence on the cycling numbers of the capacity. At the current rates of 1 C, 2 C, and 5 C, the LTO-400 sample is able to provide 99%, 98% and 97% of the capacity obtained at 0.1 C. The rate performance of the LTO-400 sample is of advantage over those of the LTO-600 and LTO-800 samples. These results demonstrate that the mesoporous structure of the LTO-400 nanoclusters is also beneficial for the enhanced rate capability. We also compare the rate performance of these samples with the commercial LTO sample. At the current rates of 1 C, 2 C, and 5 C, the commercial LTO sample can only provide 86%, 82%, and 74% of the capacity obtained at 0.1 C. It is interesting that even though the LTO-600 and LTO-800 do not show much advantage over the commercial powder at low cycling rates of 0.1 C, their high-rate capacities at 1 C, 2 C, and 5 C show great advantage over the commercial LTO powder. The better high-rate performances of LTO-600 and LTO-800 than the commercial LTO are attributed to their nano-sized dimension, which provides shorter electron and lithium ion diffusion path and favors high-rate charging/discharging processes.

As discussed above, the LTO-400 sample demonstrates better cycling and rate performance than the LTO-600, LTO-800, and commercial LTO samples. To further investigate the cycling stability

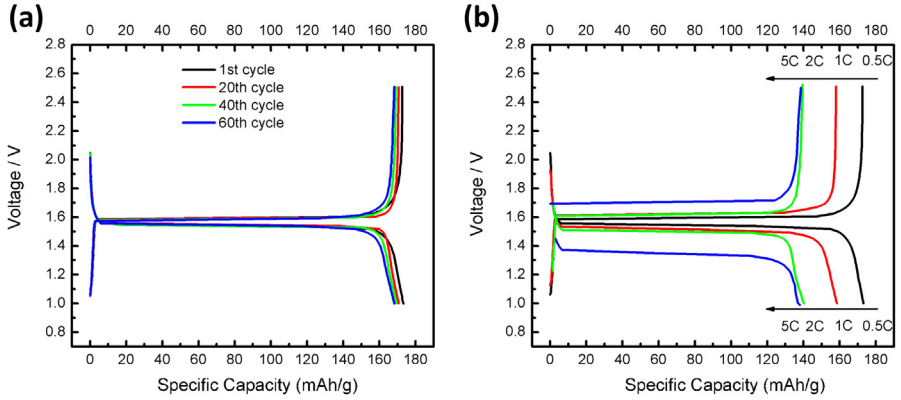

Fig. 6. (a) The galvanostatic charge–discharge curves of the LTO-400 sample. The cycling rate is 0.5 C, the charge/discharge curves of the 1st, 20th, 40th and 60th cycle are plotted. (b) The galvanostatic charge-discharge curves for the LTO-400 sample at the rates of 0.5 C, 1 C, 2 C, and 5 C.

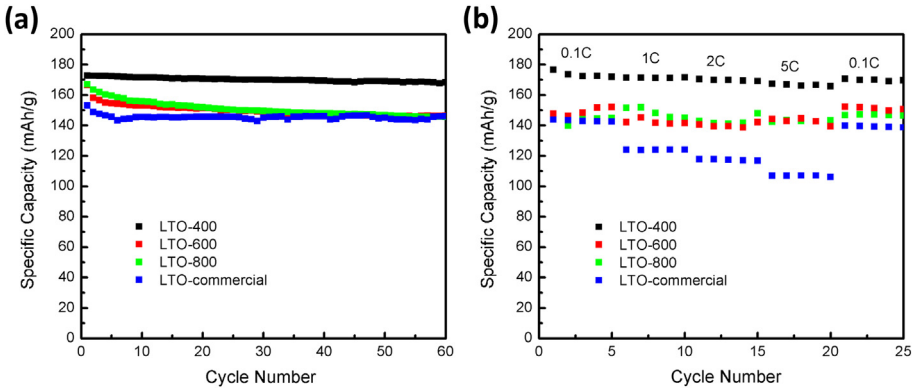

Fig. 7. (a) Cycling (0.5 C) and (b) rate (1 C, 2 C, and 5 C) performance of the LTO-400, LTO-600, LTO-800, and the commercial LTO powder.

of the LTO-400 sample at high current rates, cycling tests at 1 C, 2 C, and 5 C up to 100 cycles were performed. As shown in Fig. 8(a), the LTO-400 sample presents large initial discharge capacities of 159 mAh g^{-1}, 140 mAh g^{-1}, and 138 mAh g^{-1} at the rates of 1 C, 2 C and 5 C, respectively. Besides, excellent capacity stability was also observed during these high-rate cycling processes. Even after the 100th cycle, the discharge capacities still remained at 152 mAh g^{-1}, 132 mAh g^{-1}, and 122 mAh g^{-1} for the charge/discharge rates of 1 C, 2 C, and 5 C, corresponding to fading rates of only 0.044%, 0.057%, and 0.116% per cycle. For comparison, the LTO-600 sample delivers lower capacity and poor cycling stability. The initial capacities of the LTO-600 electrodes are only 140, 136 and 132 mAh g^{-1} at the rates of 1 C, 2 C and 5 C, respectively (Fig. 8(b)). After 100 cycles, these values drop to 133, 126, and 114 mAh g^{-1} accordingly, corresponding to fading rates of 0.050%, 0.074%, and 0.136% per cycle. As stated before, the LTO-400 and LTO-600 samples are of the same particle size of 50–100 nm, and the only difference between them lies in the meso-morphology. The LTO-400 sample is featured with inner mesoporosity within its particles, while the LTO-600 is consisted of dense and non-porous particles. So we can attribute the good high-rate performance of LTO-400 to its special mesoporous structure. The same high rate charge/discharge test is also conducted to the LTO-800 and the commercial LTO powders, and the results are given in Fig. S1. After 100 cycles, the capacities were about 132(1 C), 117(2 C), 109(5 C) mAh g^{-1} for the LTO-800 sample (Fig. S1(a)) and only 130, 104, and 56 mAh g^{-1} for the commercial LTO powder (Fig. S1(b)). The capacity data of the LTO-commercial electrodes also showed large fluctuation, which was caused by the unstable electrochemical process of the large $Li_4Ti_5O_{12}$ particles at high charge/discharge rates. Note that though the LTO-600 and LTO-800 electrodes display smaller cycling stability at high current rates than the LTO-400 electrode, they both gives much larger discharge capacities and better cycling stability than the commercial LTO samples. As discussed previously, such superiority in cycling stability at high rate of the LTO-400, LTO-600 and LTO-800 samples than the commercial LTO powder is attributed to their smaller particle size and consequently shortened electron and lithium ion transportation path.

Based on the above electrochemical measurements, it is obvious that the LTO-400 sample with nanosized particles and novel mesoporous structure is beneficial when used as an electrode material for LIBs. It possesses large cycling capacity (173 mAh g^{-1} at 0.5 C), outstanding cycling stability and excellent rate capability. The superior electrochemical performance is attributed to its novel structures: (i) The LTO-400 sample possesses mesoporous structure with higher surface area than the LTO-600 and LTO-800 samples. The high surface area of its porous network within the electrode allows numerous channels for electrolyte infiltration and facilitates the migration of lithium ions between the active material particles and electrolyte. (ii) The LTO-400 nanoclusters are of smaller dimension of 50–100 nm, which, to some extent, alleviate the problems of slow electrochemical kinetics by offering shortened electron/ion transport pathways during the lithium intercalation/deintercalation processes. To work as a negative electrode material, the LTO-400 sample combines the advantage of mesoporosity and nanodimension, which then provides excellent electronic conduction, short charge carrier (both electrons and lithium ions) transport path lengths, and easy access of the electrolyte to the increased surface area, leading to excellent lithium-ion battery performance.

The electrochemical performance of the LTO-400 sample (173 mAh g^{-1} at 0.5 C) is above or competitive with those of previously reported $Li_4Ti_5O_{12}$ negative electrodes with nanosized

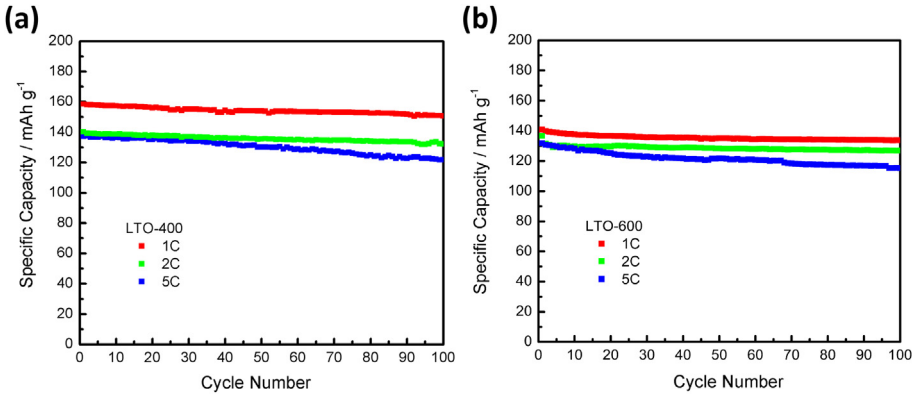

Fig. 8. The cycling performance of the (a) LTO-400 and (b) LTO-600 at the charge/discharge rates of 1 C, 2 C, and 5 C.

particles and porous structures. Prakash et al. fabricated nanocrystalline $Li_4Ti_5O_{12}$ and demonstrated a capacity of 170 mAh g^{-1} at 0.5 C, comparable to our results. However, a complex solution-combustion synthesis method and a high thermal treatment of over 800 °C were required [18]. There were also some other porous $Li_4Ti_5O_{12}$ structures reported in literature, represented by the $Li_4Ti_5O_{12}$ microspheres [21], the porous $Li_4Ti_5O_{12}$ coated with N-doped carbon [3], and the recent $Li_4Ti_5O_{12}$ hollow spheres [30]. Though these porous $Li_4Ti_5O_{12}$ structures effectively functioned in improving the rate capability and a stable capacity of around 160 mAh g^{-1} was revealed at 0.5 C, their synthesis procedures usually needed complex methods (hydrothermal treatment, spray drying, templating approach etc), inert atmosphere (Ar), or high-temperature heat treatment (mostly higher than 700 °C). While the synthetic route introduced in this article is facile and inexpensive, characterized by a simple calcination process at low temperature. The calcination temperature of 400 °C is lower than those used in previous synthesis of spinel-phased $Li_4Ti_5O_{12}$ [3,18,21,23], which is considered as a reservation of energy, thus benefiting the large-scale production.

4. Conclusions

$Li_4Ti_5O_{12}$ nanoclusters with mesoporous structure have been successfully fabricated for use as high rate negative electrodes. The nanoclusters enable delithiation/lithiation in active material within a very short time. The high porosity and large surface area of the $Li_4Ti_5O_{12}$ particles provide easy access of electrolyte to the active material. Such porous $Li_4Ti_5O_{12}$ nanoclusters deliver a high initial capacity of 173 mAh g^{-1} at 0.5 C and a high retention of the capacity (162 mAh g^{-1} after 60 cycles). It also offers an excellent cycling behavior at higher rates. Moreover, the synthesis of the $Li_4Ti_5O_{12}$ nanoclusters requires heat treatment in air at temperature as low as 400 °C, which demonstrates a simple and effective approach to synthesize $Li_4Ti_5O_{12}$ for high-performance electrochemical energy storage.

Acknowledgments

This work was supported by the National Basic Research Program of China (2012CB932301) and the NSFC (51102146).

Appendix A. Supplementary data

Supplementary data related to this article can be found at http://dx.doi.org/10.1016/j.jpowsour.2013.09.041.

References

[1] S.S. Zhang, J. Power Sources 161 (2006) 1385–1391.
[2] T. Kar, J. Pattanayak, S. Scheiner, J. Phys. Chem. A 105 (2001) 10397–10403.
[3] L. Zhao, Y.S. Hu, H. Li, Z. Wang, L. Chen, Adv. Mater. 23 (2011) 1385–1388.
[4] M.M. Thackeray, P.J. Johnson, L.A. De Picciotto, P.G. Bruce, J.B. Goodenough, Mater. Res. Bull. 19 (1984) 179–187.
[5] K.M. Colbow, J.R. Dahn, R.R. Haering, J. Power Sources 26 (1989) 397–402.
[6] E. Ferg, R.J. Gummov, A. de Kock, M.M. Thackeray, J. Electrochem. Soc. 141 (1994) L147–L150.
[7] T. Ohzuku, A. Ueda, N. Yamamoto, J. Electrochem. Soc. 142 (1995) 1431–1435.
[8] S. Sarciaux, A. Le Gal La Salle, D. Guyomard, Y. Piffard, Mol. Cryst. Liq. Cryst. 311 (1998) 63–68.
[9] S.I. Pyun, S.W. Kim, H.C. Shin, J. Power Sources 81–82 (1999) 248–254.
[10] S. Scharner, W. Weppner, P. Schmid-Beurmann, J. Electrochem. Soc. 146 (1999) 857–861.
[11] S. Panero, P. Reale, F. Ronci, V. Rossi Albertini, B. Scrosati, Ionics 6 (2000) 461–465.
[12] P. Kubiak, A. Garcia, M. Womes, L. Aldon, J. Olivier-Fourcade, P.E. Lippens, J.C. Jumas, J. Power Sources 119-121 (2003) 626–630.
[13] S.H. Huang, Z.Y. Wen, J.C. Zhang, Z.H. Gu, X.H. Xu, Solid State Ionics 177 (2006) 851–855.
[14] G.J. Wang, J. Gao, L.J. Fu, N.H. Zhao, Y.P. Wu, T. Takamura, J. Power Sources 174 (2007) 1109–1112.
[15] J. Gao, J. Ying, C. Jiang, C. Wan, J. Power Sources 166 (2007) 255–259.
[16] L. Cheng, J. Yan, C.N. Zhu, J.Y. Luo, C.X. Wang, Y.Y. Xia, J. Mater. Chem. 20 (2010) 595–602.
[17] K. Ariyoshi, T. Ohzuku, J. Power Sources 174 (2007) 1258–1262.
[18] A.S. Prakash, P. Manikandan, K. Ramesha, M. Sathiya, J.M. Tarascon, A.K. Shuakla, Chem. Mater. 22 (2010) 2857–2863.
[19] Y.G. Guo, Y.S. Hu, W. Sigle, J. Maier, Adv. Mater. 19 (2007) 2087–2091.
[20] C.M. Doherty, R.A. Caruso, B.M. Smarsly, P. Adelhelm, C.J. Drummond, Chem. Mater. 21 (2009) 5300–5306.
[21] L. Shen, C. Yuan, H. Luo, X. Zhang, K. Xu, Y.J. Xia, J. Mater. Chem. 20 (2010) 6998–7004.
[22] J.Q. Qi, L. Sun, X.W. Qi, Y. Wang, H.L.W. Chan, J. Solid State Chem. 184 (2011) 2690–2694.
[23] Y.F. Tang, L. Yang, Z. Qiu, J.S. Huang, J. Mater. Chem. 19 (2009) 5980–5984.
[24] W.J. Thomas, B. Crittenden, Adsorption Technology and Design, Elsevier Science& Technology, 1998, pp. 33–37.
[25] W. Xu, X.L. Chen, W. Wang, D. Choi, F. Ding, J.M. Zheng, Z.M. Nie, Y.J. Choi, J.G. Zhang, Z.G. Yang, J. Power Sources 236 (2013) 169–174.
[26] K.M. Kim, K.Y. Kang, S. Kim, Y.G. Lee, Curr. Appl. Phys. 12 (2012) 1199–1206.
[27] L.X. Yang, L.J. Gao, J. Alloys Compd. 485 (2009) 93–97.
[28] H.F. Ni, L.Z. Fan, J. Power Sources 214 (2012) 195–199.
[29] A. Jaiswal, C.R. Horne, O. Chang, W. Zhang, W. Kong, E. Wang, T. Chern, M.M. Doeff, J. Electrochem. Soc. 156 (2009) A1041–A1046.
[30] L. Yu, H.B. Wu, X.W. Lou, Adv. Mater. 25 (2013) 2296–2300.